RXTE Observations of QPOs in the Black Hole Candidate GRS1915+105

E. H. Morgan, R.A. Remillard
Center for Space Research, MIT, Cambridge, MA 02139, USA

J. Greiner
Max-Planck-Institute for extraterrestrial Physics, 85740 Garching, Germany

ABSTRACT

We report on quasiperiodic oscillations (QPOs) in the black hole candidate GRS 1915+105 seen in 31 PCA observations made by the *Rossi X-ray Timing Explorer* . We distinguish 3 different types: a QPO with constant centroid frequency of 67 Hz, dynamic low-frequency (10^{-3} to 10 Hz) QPO with a large variety of amplitudes and widths, and high-amplitude "sputters" at frequencies of 10^{-3} to 10^{-1} Hz, that are among the most extreme X-ray variations ever seen. We discuss the 67 Hz QPO with an assumption that it arises in the inner accretion disk of a black hole binary. If this QPO represents the rotation frequency of the innermost stable orbit around a non-rotating black hole, then the implied mass is 33 $M_{\odot}$. An alternative interpretation as g-mode oscillations in the inner disk (Nowak *et al.* 1996) implies a black hole mass of 10 $M_{\odot}$. Four selected QPOs at lower frequencies (0.067–1.8 Hz) are tracked continuously in 5 energy bands. The QPO-folded profiles are mostly sinusoidal. Remarkably, all four investigated QPOs are broadened in frequency by a random walk in oscillation phase. At higher photon energies the QPO profiles show larger amplitude and increasing phase lag. Our QPO profile analysis concludes that the phase delays are not caused by scattering effects, and we discuss a more direct relation between these QPOs and the origin of the hard X-ray spectrum. There are at least three general shapes to the broad-band power continuum, with a typical persistence time scale of several weeks. The combined characteristics of the power spectra, light curves, and energy spectra during the time period of 1996 February 21 to August 15 are interpreted as a succession of four different emission states. None of these appears identical to any of the canonical states of black hole binaries.

Subject headings: GRS 1915+105 — QPO — black holes — X-ray transient — accretion disk — superluminal motion — jet

1. Introduction

The black hole candidate GRS 1915+105 (Castro-Tirado *et al.* 1992) is one of two known galactic X-ray sources that exhibit superluminal radio jets (Mirabel and Rodriguez 1994). The combination of relativistic constraints and radio measurements in H I indicate that the source lies behind the Sagitarius arm at a distance of 12.5 $\pm$1.5 kpc (Mirabel & Rodriguez 1994). Interstellar extinction limits optical/IR studies to weak detections at wavelengths $>$ 1 micron (Mirabel *et al.* 1994). The source is suspected to be a black hole binary due to the spectral and temporal similarities with the other galactic X-ray source with superluminal radio jets, GRO J1655-40 (Zhang *et al.* 1994), which has a binary mass function indicative of a black hole system (Bailyn *et al.* 1995).

GRS 1915+105 is a transient X-ray source. The two previous outbursts, as seen with BATSE (25–100 keV), occurred from 1992 August until 1993 September (Harmon *et al.* 1992) and from 1993 December until 1994 April. When the ASM on *RXTE* established continuous coverage on 1996 February 21, an outburst at 2–12 keV was already well underway (Levine *et al.* 1996), although it was not detectable with BATSE until 1996 May 24 (Zhang *et al.* 1996). Starting on 1996 April 6, GRS 1915+105 has been observed with the pointing instruments of the *Rossi X-Ray Timing Explorer* (*RXTE*; Bradt, Rothschild and Swank 1993) once or twice a week. The light curves and preliminary spectral analysis of the observations through 1996 June are discussed in an earlier paper (Greiner, Morgan & Remillard 1996; hereafter paper 1). The source occasionally exhibits a sequence of extreme variations, described as brightness "sputters", in which the X-ray intensity drops by a factor as large as 4 on a time scale of a few seconds, while the spectrum softens. The X-ray luminosity (2–60 keV) reaches $10^{39}(D/12.5kpc)^2$ erg s^{-1}, which exceeds the Eddington limit for a neutron star. There is evidence of a correlation between higher X-ray flux and the presence of brightness sputters, while radio emission was reported soon after an event of chaotic X-ray variability. These relations were noted to suggest that the formation of radio jets may be caused by an accretion instability in the inner disk.

In the present paper we continue the analysis of *RXTE* observations of GRS 1915+105. We investigate the power spectra of 31 PCA observations in order to characterize the X-ray states of this remarkable source and to investigate the rich variety of quasi-periodic oscillations (QPOs) apparent in the X-ray emission. Previous studies of accreting black hole binaries suggest a hierarchy of X-ray states (off, low/hard, high/soft and very high) in which the spectral and temporal properties are governed primarily by the rate of mass accretion (Tanaka and Lewin 1995: van der Klis 1995). X-ray investigations of GRS 1915+105 are thus motivated by several interrelated purposes: to search for clues regarding the origin of relativistic jets, to characterize the emission of an X-ray binary in a very high state, and to

probe the emission for clues regarding the nature of the compact object.

2. Observations and Analysis

We present the results of 31 observations of GRS 1915+105 made between 1996 April 6 and 1996 August 31 using the RXTE Proportional Counter Array (PCA; Jahoda *et al.* 1996). A summary of these observations is given in Table 1. For reference, Figure 1 contains the long term X-ray light curve of GRS 1915+105 from the RXTE All Sky Monitor (ASM; Levine *et al.* 1996), and the time of each PCA observations is shown with a vertical dash near the top of this figure. The PCA observations are typically 10 ks exposures with gaps due to earth occultation, satellite passage through the South Atlantic Anomaly (SAA), and in some cases brief observations of another target.

All observations, except for the first 4, were made using the same EDS configurations. All high energy photons (> 13.3 keV; channel 36) were telemetered individually with a time tag accurate to 15 μs (2^{-16} s) and with 16 energy channels in "event mode". The low energy photons were telemetered in 2 ways: a multi-channel binned mode with 2 ms time resolution and a single channel (single-bit mode) with 61 μs resolution. On the ground the high energy photons from event mode were binned and analyzed in conjunction with the binned mode and single-bit mode data. The first two observation were made before the gain in the PCA proportional counters was lowered by $\sim 35\%$ on 1996 April 15 (Jahoda *et al.* 1996), causing a shift in the linear relation between PHA bin and photon energy. Before April 15, PHA bin 256 corresponded to ~ 60 keV, while afterwards it corresponds to ~ 90 keV. The first 4 observations were made with a similar strategy, but the boundary between event and binned mode was at channel 50 (18 keV after the gain change), the binned mode had 16 energy channels with 16 ms time resolution and the event mode had 61μs time resolution with 32 energy channels.

For each observation we constructed the power density spectrum (PDS) by piecing together results from two different analyses. For frequencies below 1 Hz the PDS was calculated using a single Fourier transform on counts in 0.125 s time bins over the entire observation. The gaps in the data were filled with the mean and the resulting PDS was rescaled by the filling factor (i.e. the number of bins in transform/number of exposed bins). Above 1 Hz the PDS is generated by summing many transforms of data with time bins of 61 μs. The low frequency and high frequency PDS were compared in the region where they overlap to ensure consistency before splicing the two pieces together.

The Poisson noise level was subtracted using equation 24 from Zhang *et al.* (1995)

for the instrument dead time, assumed here to be purely paralyzable, plus the effect of Very Large Events (VLE) (Zhang *et al.* 1996). We used the following formula for the deadtime-corrected Poisson level:

$$P(\nu) = 2[1 - 2r_0\tau_d(1 - \frac{\tau_d}{2t_b})] - 2\frac{N-1}{N}r_0\tau_d(\frac{\tau_d}{t_b})cos(2\pi t_b\nu) + 2r_{vle}r_0\tau^2(\frac{\sin(\pi\tau_{vle}\nu)}{\pi\tau_{vle}\nu})^2, \quad (1)$$

where r_0 is the count rate per PCU, r_{vle} is the rate of VLE events per PCU, t_b is the time bin size (e.g. $2^{-14}s \cong 61$ μs), N is the number of frequency points (524288), τ_d is the deadtime per event, which is 10 μs for the PCA. The deadtime window for each VLE event, τ_{vle}, was set to 170 μs for most of the observations, and to 70 μs for May 26, June 16 and all observations after August 3. Note that the Poisson level depends on the frequency. This effect is clearly seen in the PDS of every bright source observed with *RXTE* at high time resolution. We find that this method underestimates the Poisson noise level by values $\leq 0.5\%$ of the mean rate.

3. Results

The ASM light curve and hardness ratio plots are shown in Figure 1, with analysis methods described in detail by Levine *et al.* (1996). HR1 is the ratio of flux at 3-5 keV to the flux in the 1.3-3 keV band, while HR2 is the ratio of 5-12 keV flux to the 3-5 keV flux. The appearance of the ASM light curve suggests 4 different emission states, and in subsequent sections we will show that the PCA power spectra and QPO properties also change characteristics as the source migrates through these states. For the purpose of discussion, we label these 4 states (see labelling in Figure 1): chaotic, bright, flaring, and low-hard. Prior to MJD 50170 (March 28), the ASM light curve is incredibly variable ("chaotic state"), with a sample distribution 0.66±0.24 Crab at 2-12 keV, while a comparatively soft X-ray spectrum is suggested in the mean values, HR1 = 1.90 and HR2 = 1.32. The MJD interval 50170-50220 (March 28 – May 17) appears as a bright and fairly steady state with an average ASM flux (2-12 keV) of 1.1 Crab and hardness ratio values, HR1 = 2.18 and HR2 = 1.39 (statistical uncertainty ±0.02). The interval 50220-50280 (May 17 – July 16) appears in the ASM as a flaring state with similar hardness ratios (2.08, 1.31), but a very different light curve in which the source flares by factors as large as 6 with time scales up to several days. Finally, during he interval 50280-50310 (July 16 – August 15) the ASM reveals a remarkably steady, low state, with average daily flux of 0.51±0.02 Crab and very different hardness ratios: HR1 = 1.82 and HR2 = 1.74. We note that the spectrum is very hard during this time, and the lower ASM count rate (2-12 keV) does not necessarily imply lower luminosity. After MJD 50310 GRS 1915+105 appears to return to

the flaring state.

In Figures 2 through 5, we present the PDS of the 31 PCA observations, with results plotted logarithmically. We discuss the general characteristics of the power spectra in four subsections below. PCA light curves for some of the early observations of GRS 1915+105 are presented in paper 1.

3.1. 67 Hz QPO

Perhaps the most unexpected feature seen in the PDS is a sharp QPO seen at 67 Hz in several observations, particularly in late April and early May. A careful examination of all 31 observations reveals six cases in which the feature at 67 Hz is detected. The power density spectra of these six observations, plotted linearly in the range 25 to 200 Hz, is shown in Figure 6. Here we have not subtracted the Poisson noise level. In Table 2 we list the parameters derived from fitting the QPO feature with a Lorentzian profile. The variations in the centroid frequency are only 1 Hz. The feature is very sharp, with $Q \approx 20$, where Q is defined to be the ratio of the QPO line centroid to the line width. The RMS amplitude is between 0.5 and 1.6%. For the observations where the QPO is not detected, the 99% confidence upper limit on the RMS is typically 0.3–0.4% depending on the exposure and count rate.

In Figure 7 we show the energy dependence of the 67 Hz QPO from the May 5 observation. The RMS amplitude is clearly increasing with photon energy, from a level of 1.5% below 5 keV to 6% above 13 keV. This relation clearly associates the 67 Hz QPO with the most energetic spectral components visible to the PCA.

3.2. QPOs between 10^{-3} and 10 Hz and X-ray States

In the observations of GRS 1915+105 (see Figures 2-5) we find a diverse assortment of QPOs between 1 mHz and 10 Hz. These QPOs are dynamic, changing frequency on time scales of minutes. In Table 1 we have listed the centroid frequency for the strongest QPOs in each observation. A thorough description of the diverse and complex QPO features of GRS 1915+105 presents a formidable challenge. However, there is a gradual evolution in both the QPO properties and the shape of the broad-band power continuum, and this evolution is correlated to the appearance of the ASM light curve. This organization in source behavior provides a framework for assessing both the QPOs and the X-ray states of GRS 1915+105, although we note there are no PCA observations during the chaotic state.

In the PCA power spectra before May 20, when the source is in the bright state, there is a rich combination of both broad and narrow QPO ($1 < Q < 50$) in the range of 1 mHz to 10 Hz. This time interval is also characterized by high PCA count rates (1–3 Crab) and modest values in the integrated broad-band power (10–15%; see Table 1). This interval is also one in which the 67 Hz QPO is detected most often. We see no simple relation between the frequencies of the broadest and narrowest QPOs, nor between QPO frequencies and the other emission properties listed in Table 1. This time interval is also associated with a broad-band power continuum that can be described as a "wobbly" power law, often showing a very broad knee that is centered near 1 Hz. When the deviations from a power law continuum are least significant, e.g. in the range of 0.1–100 Hz on April 9, the power-law index is modestly steep with a value near 1.5.

Between May 21 and July 6, inclusive, and correlating with the ASM flaring state, the QPOs are weak and very broad, with centroid frequencies in the range of 0.6–6 Hz and $Q < 2$. Both the average PCA count rate and the integrated RMS power during this time interval vary significantly from observation to observation. Low frequency "sputters" (see Section 3.3 below and paper 1) were often apparent. The power continuum during these observations may have a slightly flatter distribution, e.g. with a power-law index of 1.14 in the range of 0.1–100 Hz on June 29).

Beginning on July 11, when the source begins a transition to the low-hard state, we observe another important change in the PCA power spectra (see Figs. 4 and 5). All of the PDS during this time are distinguished by a broken power-law in the broad-band continuum, with a typical power-law index of 0.0 between 0.01 and 1.0 Hz, switching to a value of 2.5 in the range 3–100 Hz. Strong QPOs emerge in the range of 0.6 to 8 Hz, lying near the break point in the slope of the broad-band power continuum. Therefore, whatever is causing this QPO appears to additionally function as a low-pass filter on X-ray variations from GRS1915+105 during this "low-hard" emission state. If these data are subdivided, e.g. by satellite orbit, then the corresponding power spectra show narrow QPOs ($Q \approx 20$) with variable centroid frequencies. For example, in the July 11 observation, the PDS shows 2 distinct peaks, and these arise from a shift in the centroid frequency from 3.5 Hz in the first orbit to 2.5 Hz in the third orbit. During this time interval the PCA count rates are notably steady and the mean hardness ratio is comparatively high (see Table 1).

3.3. Wave Form and Energy Dependance of QPOs

In many QPO in GRS 1915+105 we see one or more harmonics of the fundamental frequency. The most extreme case is the May 5 observation in which the narrow QPO at

0.067 Hz (15 s) and its first 3 harmonics are clearly seen. The harmonics in the power spectra are due to the shape of the modulation, which are individually seen in a series of narrow dips (2–4 s wide) in the light curves. To begin the investigation of the wave forms and energy dependence of the QPOs we chose several observations with strong QPO and divided the light curves into 5 energy channels ($< 5.2, 5.2$–$7.0, 7.0$–$9.6, 9.6$–$13.3, > 13.3$ keV, respectively). We then computed the power spectrum for each channel. The results, presented in Figure 8, show differences in the energy dependence of QPO profiles. For the narrow QPOs seen at 0.06–0.20 Hz on April 29 and May 5, the power in the harmonics, relative to the power in the fundamental, increases with higher photon energy. However, for the broader QPOs seen on May 14, July 16, July 26, and August 3, the opposite relation applies as the first harmonic is stronger in the lower energy channels.

To further investigate the various X-ray QPO in GRS 1915+105 we utilize the high count rates of these *RXTE* observations to track the QPO phase continuously and to determine the mean oscillation profiles in different energy bands. We performed this analysis on the 0.067 Hz QPO of May 5, the 0.114 Hz QPO of May 14, the 0.65 Hz QPO of July 26 and the 1.8 Hz QPO of August 8. Sample light curves selected from these four observations are presented in Figure 9. The individual QPO oscillations are clearly seen in the time domain in each case.

We measure the phase and amplitude of each oscillation as follows. We first examine the light curve and choose a template function, which consists of a constant plus a suitable wave feature (e.g. a sine wave). We then fit the template to the data in a window that slides in time in a series of small quantized steps. The width of the window is the mean period of the QPO, and the free parameters for each fit are the template's constant and the amplitude of the chosen waveform. The derived amplitudes display local maxima whenever the template is in phase with the QPO waves in the light curve. For maxima above a chosen threshold, we compute parabolic fits to interpolate the best value for the time and amplitude of each maximum, and these values then serve as the arrival time and amplitude for the individual QPO wave. The resulting time line of wave properties may then be analyzed for autocorrelation and phase-amplitude correlation. We also co-add the oscillations, re-centering the phase for each wave's arrival time, to produce the mean "QPO-folded" wave form. Before this analysis is concluded, we must obtain consistency between the template function and the final QPO-folded wave form. We start the analysis using a sine wave for the template function. If the derived QPO-folded wave form deviates significantly from a sine wave, then a new template function is chosen and the process is iterated until the template function reasonably matches the mean QPO wave form.

The QPO at 0.067 Hz on May 5 was tracked with a template consisting of a constant

plus and inverted Gaussian of width $\sigma = 1.4$ s. The template is therefore a Gaussian dip with a FWHM of 3.3 s and a mean recurrence time of 14.93 s. We successively fit this template to the light curve (2-20 keV) in 0.125 s steps, and we interpolated the arrival time and amplitude of each QPO wave as described above. More than 94% of the expected QPO waves are retrieved in the PCA light curve, and the results are shown in Figure 10. The top panel contains the arrival times of each QPO dip, modulo the mean QPO period. Within the intervals of continuous coverage there are few instances in which a phase jump is larger than 3 s (or 0.2 in phase). The data gaps are associated with the satellite orbit. The number of QPO cycles across a gap is unknown, and so we artificially chose the minimum phase offset to relate the first dip after a gap to the previous observed dip. The bottom panel in Figure 10 tracks the dip amplitude, represented as a fraction of the average flux for the full energy range of the PCA instrument. The dip amplitudes have a uncorrelated scatter, with a Gaussian distribution centered at 15% and $\sigma = 3\%$. The time between adjacent QPO minima also exhibits uncorrelated scatter with a Gaussian distribution centered at 14.93 s with $\sigma = 0.72$ s. Furthermore, there is no correlation between the QPO separation time and the amplitude of the wave. These statistical results establish the conclusion that the frequency width of the QPO at 0.067 Hz on May 5 is entirely due to a random walk in the phase of the individual oscillations.

Using the arrival times from Figure 10, we computed the mean "QPO-folded" profile for the 0.067 Hz QPO of May 5 in 5 energy bands (those described previously), and the results are shown in Figure 11. The PCA background values have been subtracted in each band, although the values are less than 1% of the flux from GRS1915+105 except for the highest energy band. The 3 s dip appears in each energy interval, and the amplitude of the dip varies smoothly from 16% of the mean flux in the 2–5.2 keV band(top panel) to 28% at energies above 13.6 keV (bottom panel). There is also a clear time delay that systematically increases with higher energy; the top and bottom panels are offset by 0.64 s (4.3%). This QPO was noted as showing harmonics with increased strength at higher photon energy, and here we see sharper features in the lower panels of Figure 10, including a strong secondary minimum.

We track the 0.11 Hz QPO on May 14 in a similar manner, using a template function consisting of a constant plus a sine wave with the mean QPO frequency. The arrival times and amplitudes are shown in Figure 12. Again, the QPO arrival times display a random walk, and we find no correlation between QPO separation time and amplitude. The width of the Gaussian distribution in the times between adjacent QPO minima is 1.3 s. The QPO-folded profile is shown in the 5 energy bands in Figure 13. This QPO profile is quite different from the May 5 QPO, and the delay with higher energy is smaller, with a time lag of 0.16 s between the lowest and highest PCA energy channels. We note that there is a weak

QPO at 0.012 Hz during this observation, and this induces a detectable modulation in both the amplitude and arrival times shown in Figure 12. However, this should not influence the QPO profile shown in Figure 13. The mean QPO amplitude, measured minimum to maximum, is 18% of the mean flux in the 2–5.2 keV band(top panel), gradually rising to 43% at energy > 13.6 keV (bottom panel).

Shifting attention to QPO during the "low-hard" state, we track the 0.65 Hz QPO of July 26, again using the sine wave template. The arrival times and amplitudes are shown in Figure 14, and this QPO resembles the May 14 case in all respects, except for the change in frequency and the accelerated gradient of the random walk in the QPO arrival times (typical drifts up to 13 phase units per 1000 s in this case). The QPO-folded profiles per energy band are shown in Figure 15. This is the most sinusoidal QPO among those analyzed in detail, and this case is an example of a QPO with increasing structure at lower photon energy. The amplitudes again vary with photon energy (25% to 32%). The time lag at higher energies remains positive, with a delay of 0.086 s between the top and bottom panels of Figure 15.

Finally, we track the 1.8 Hz QPO from August 10. The mean QPO centroids for the 3 *RXTE* orbits are located at 1.69, 1.88 and 1.98 Hz, respectively. The QPO frequencies for August 10 (and nearby dates) are listed in Table 1 as a range of results, since the QPO frequency varies significantly between each *RXTE* orbit. Despite the higher frequency, our analysis continues to retrieve the great majority of expected QPO waves (96% in this case). The results (not shown) are very similar to the QPO of July 26, with a sinusoidal form, characteristic amplitudes of 24–44% (greater at higher energy), and further accelerations in the time scale for phase drift. The width of the distribution in the times between adjacent minima is 0.056 s. The time lag from 3 to 15 keV for these QPO is 0.018 s, amounting to a typical phase delay of 3.3% over a span of 12 keV.

3.4. Low frequency-high amplitude QPO

In paper 1 we describe high amplitude variations in the light curves of GRS1915+105 as brightness "sputters" and illustrate such episodes on 1996 April 6, May 26 and June 19. It is clear in the light curves that these episodes occur as a hierarchy of high-amplitude, low-frequency QPOs. In Figures 2 and 3 above, the power spectra on these dates do not show distinct low frequency QPO; however, the sputters are represented in the broad excess in power with values > 1 $(rms/mean)^2 Hz^{-1}$ in the range of 0.001–0.1 Hz. This criterion identifies six additional episodes of brightness sputters (intensity max./min. > 2) that are represented in the power spectra (see Figures 2–5) of May 21, June 12, 16, 22, 25, and

July 6. In the present paper we limit our discussion of brightness sputters, noting their recurrence and their impact on the power spectra of GRS1915+105. Additional analyses of these highly complex phenomena and their relationship to the times of radio outbursts is an ongoing research effort that will be reported in a later paper.

4. Discussion

One of the major questions applied to observations of X-ray binaries is whether these sources behave as photon "engines" that traverse well-defined states. Such investigations typically search for combined spectral and variability properties that reveal a patterned response to changes in accretion, particularly the mass accretion rate (van der Klis 1994). In the case of GRS1915+105, we have described the X-ray power spectra as showing 3 separate types (no PCA coverage of the chaotic state), each occurring in successive time intervals that persist for several weeks.

There is great difficulty relating these patterns of emission from GRS1915+105 with the "low/hard", "high/soft" and "very high" states commonly described for black hole binaries (van der Klis 1995). In an absolute sense, the ASM HR2 values for GRS1915+105 in all 4 intervals are "harder" than the Crab (for which HR2 = 1.19), suggesting a "flat" energy spectrum usually seen as a power-law that is interpreted as inverse Compton emission in which thermal photons are boosted into hard X-rays by energetic electrons. In the typical black-hole X-ray binaries, this spectral component is strongest in either the "low" or "very high" states. Our "low-hard" state for GRS1915+105 shows strong QPO at 1-10 Hz, which is a defining characteristic of the canonical "very high" state (van der Klis 1995; Miyamoto *et al.* 1991; 1993). Since the remaining intervals for GRS1915+105 are brighter and more variable, all of the four GRS1915+105 states could be super-variants of the very high state. On the other hand, our flaring interval exhibits a light curve and a (roughly) 1/f power spectrum that resembles Cyg X-1 in its high state (Cui *et al.* 1996), but the energy spectrum is very different. Further confusion arises if we note that the low-hard state of GRS1915+105 (with hardest HR1 values, lowest flux, and a power spectrum with a broken power-law shape) are reminiscent of the canonical low/hard state, except for the presence of QPOs. Overall, the phenomenology of GRS1915+105 variability perhaps resembles the diversity seen in Cir X-1, believed to be a neutron star system which also exhibits episodes of bright and highly unstable emission in X-rays (Oosterbroek *et al.* 1995). The diverse power spectra from Cir X-1 resemble those from GRS1915+015 in some respects, particularly the type in which a broken power law shows a QPO at the transition frequency (Shirey *et al.* 1996). We conclude that the efforts to force the interpretation of GRS1915+105 properties

in terms of canonical states are currently unproductive; efforts will be made to search for repetitions of the four behavior patterns while the current outburst proceeds.

In Section 3.2 we described results obtained by individually tracking the oscillations in four QPO wave trains. We selected QPOs that span a factor of 25 in frequency (0.067–1.8 Hz), with samples that arise from two different states. Three of these cases have a mean QPO-folded wave form that is essentially sinusoidal, (in contrast to the "dip" form of the slowest QPO), while all four QPOs show time lags at higher energy, with a characteristic phase lag of 0.03 between 3 and 15 keV. All of the QPO amplitudes (measured minimum to maximum) cluster around 15% of the mean flux, and the amplitudes increase with higher photon energy (within 3–15 keV). Since the similarities are more striking than the differences here, these QPOs may have a common origin, despite the differences in frequency and their association with two different emission states.

The cross spectrum computed for GX339-4 (Miyamoto *et al.* 1991) and GS1124-68 (Miyamoto *et al.* 1993) show phase lags at higher energy, in a statistical sense, which are similar to the time delays in the energy-resolved QPO-folded profiles shown above for GRS1915+105. The ability to track the individual QPO waves with the PCA provides additional constraints for physical models for these delays. The previous studies hypothesized that the QPOs could arise from inner disk oscillations, and they interpret the time delays as effects due to Compton scattering in a hot cloud of radius $\sim 10^9$ cm surrounding the compact object. In the present study, the time delay for the slowest QPO is 0.6 s between 3 and 15 keV, but the mean wave form does not exhibit the profile smearing that certainly would be detected in the (delayed) higher energy bands if the scattering cloud were a spherical halo with a characteristic radius up to 0.6 light s.

Alternatively, the high amplitudes revealed in the QPO-folded profiles (16–25% at 3 keV rising to 28–44% at 15 keV) as well as the sharp QPO profiles at high energies both suggest a more direct association between the QPO mechanism and the origin of the Comptonizing electrons. The QPO delay time at higher energies is far longer than the Keplerian time scale for the hottest regions of the accretion disk, and so we speculate that the QPO oscillations originate in some other structure associated with the creation of energetic electrons, e.g. in the geometric boundary between the inner disk and the hot advecting gas in the advection model (Narayan 1996), or in the location of a shock front that operates in some accretion models (e.g. Chakrabarti & Titarchuk 1995). Such geometric oscillations in GRS1915+105 might be influenced by radiation near the Eddington limit. Alternatively, the electrons could be produced in an oscillatory manner as part of the jet formation mechanism. In any case, the QPO amplitudes and frequency impart serious contraints on the radius of the Compton region and either the Compton cooling time scale

or the bulk motion time scale (either inward or outward) in which the energetic electrons escape the Compton seed photons.

There has been speculation (see e.g. van der Klis 1995) as to whether the QPO phenomenon is due to amplitude modulation, frequency modulation, or some other mechanism. Our result clearly shows that, in this case, the width of the QPO is due to uncorrelated phase jitter from one pulse to the next. This random walk of the QPO phase rules out most models that depend on beat frequencies between strict clocks and transient structures with patterned lines of motion, such as the QPO model for neutron-star binaries (Lamb 1988). The uncorrelated scatter in the QPO amplitudes seems to rule out models where the QPO is formed from oscillating shots of finite duration (van der Klis 1995). Finally, the lack of correlation between the amplitude and phase delay appears to rule out models based on incoherent reservoir depletion (e.g. dripping faucet type models).

The transient yet recurring high-frequency QPO at 67 Hz appears to be an entirely different phenomenon. Currently, there is no observational distinction between QPOs that occur in black hole binaries vs. those in confirmed neutron star systems. High frequency QPOs are seen in neutron star systems (e.g van der Klis *et al.* 1996, Strohmeyer *et al.* 1996), and these typically show significant variations in the centroid frequency. A notable exception is the broad QPO ($Q < 2$) seen at 37 Hz in the bursting X-ray pulsar GRO J1744-28 (Zhang *et al.* 1996). Further progress in this area will likely require many more QPO detections in the range of 10–100 Hz.

If we assume that the accreting star in GRS 1915+105 is a black hole, then a natural time scale at high frequency is the Keplerian period of the innermost stable orbit in the accretion disk. This orbit lies at 3 Schwarzschild radii (R_s) for a non-rotating black hole. The period of this orbit depends only on the mass and rotation of the black hole. Therefore there is a possibility that a fixed high-frequency feature in the power spectrum may provide constraints on the mass and rotation of the black hole. The frequency of this orbit is: $f = 2.2(M_\odot/M_{BH})$ kHz, for a Schwarzschild black hole (Shapiro & Teukolsky 1983). If the observed 67 Hz QPO is directly related to this frequency then the implied black hole mass is 33 $M_\odot$.

Models predicting vertical oscillations in black-hole accretion disks as a consequence of relativistic effects near the Schwarzschild radius have been developed by Nowak *et al.* (1996; see also Titarchuk and Lapidus 1996, Perez *et al.* 1995 and Nowak & Wagoner 1993). The frequency of the oscillations in these models also depends primarily on the mass and rotation of the black hole (variations due to other parameters are of order 1%). Nowak *et al.* (1996) interpret the 67 Hz QPO in GRS1915+105 (Nowak *et al.* 1996) as the frequency of the lowest radial g-mode oscillation in the disk, and they concluded that the mass of

the black hole is $10 M_{\odot}$, if it is not rotating. Using numerical simulations of the nonlinear time-dependent evolution of the inertial-acoustic instability, Chen and Taam (1995) have predicted QPOs with frequencies of 115-135 Hz for a 10 $M_{\odot}$ black hole. The frequency of the QPOs in these simulations depends more strongly on the mass accretion rate as well as on the mass of the black hole, so we would expect the QPO frequency to change with $\dot{M}$ if this model applies.

5. Conclusions

In summary, we have investigated quasiperiodic variability in the X-ray emission from GRS1915+105 with the *RXTE* PCA instrument. A recurrent QPO at 67 Hz is discovered. The interpretation is currently ambiguous, but this feature may hold clues about the mass and rotation of a black hole in the binary system. Four X-ray states are identified in which the combined characteristics of the light curves, power spectra, and energy spectra persist on time scales of weeks. If these are related to the common emission states of other black holes binaries, then they are variations of the "very high" state. Two states of GRS1915+105 are associated with high-Q QPOs, and our QPO-tracking analysis reveals oscillations with a random walk in phase and a distinct increase in both the amplitude and time delays with higher energy. If the high energy photons are derived from inverse Compton scattering, then the QPO-folded profiles suggest that the energy distribution of the energetic electrons must be oscillating at the QPO frequency.

We thanks Wei Cui, Al Levine, Hale Bradt, Nan Zhang, Mike Nowak and Saul Rappaport for useful comments and discussions. EM and RR are supported by NASA contract NAS 5-30612. JG is supported by the German Bundesministerium für Bildung, Wissenschaft, Forschung und Technik (BMBF/DARA) under contract FKZ 50 OR 9201. JG thanks the Deutsche Forschungsgemeinschaft (DFG) for a travel grant.

REFERENCES

Bailyn, C. D., Orosz, J. A., McClintock, J. E., Remillard, R. A., 1995, Nature 378, 157

Bradt, H. V., Rothschild, R. E., & Swank, J. H. 1993, A&AS, 97, 335

Castro-Tirado, A. J., Brandt, S., Lund, N., 1992, IAU Circ. 5590

Chakrabarti, S. K. & Titarchuk, L. G. 1995, ApJ, 455, 623

Chen, X., & Taam, R. E. 1995, ApJ, 441, 354

Cui, W., Heindl, W. A., Rothschild, R. E., Zhang, S. N., Jahoda, K., & Focke, W. 1996, ApJL, 474, L57

Greiner, J., Morgan, E. H., Remillard, R. 1996, ApJL, 473, L107

Harmon, B. A., Paciesas, W. S., Fishman, G. J., 1992, IAU Circ. 5619

Lamb, F. K. 1988, Adv Space Res, 8, 421

Levine, A. M., Bradt, H., Cui, W., Jernigan, J .G., Morgan, E. H., Remillard, R., Shirey, R. E., & Smith, D. A. 1996, ApJL, 469, L33

Mirabel, I. F., *et al.* , 1994a, A&A, 282, L17

Mirabel, I. F., Rodriguez, L.F., 1994b, Nature 371, 46

Miyamoto, S., Iga, S., Kitamoto, S., & Kamado, Y. 1993, ApJL, 403, L39

Miyamoto, S., Kimura, K., Kitamoto, S., Dotani, T., & Ebisawa, K. 1991, ApJ, 383, 784

Narayan, R. 1996, ApJ, 462, 136

Nowak, M. A., Wagoner, R. V. 1993 ApJ, 418, 187

Nowak, M. A., Wagoner, R. V., Begelman, M. C., & Lehr, D. E. 1996 ApJ, submitted

Oosterbroek, T., van der Klis, M., Kuulkers, E., van Paradijs, J., & Lewin, W. H. G. 1995, A&A, 297, 141

Shapiro, S. L., Teukolsky, S. A., 1983 "Black Holes, White Dwarfs, and Neutron Stars", John Wiley & Sons

Shirey, R. E., Bradt, H. V., Levine, A. M., & Morgan, E. H. 1996, ApJL, 469, L21

Strohmayer, T. E., Zhang, W., Swank, J. H., Smale, A., Titarchuk, L., Day, C. & Lee, U. 1996, ApJL, 469, L9

Titarchuk, L., & Lapidus, I. 1996, ApJL, submitted

van der Klis, M. 1995, in X-ray Binaries, eds. Lewin, van Paradijs, & van den Heuvel, Cambridge: Cambridge University Press, p. 252

van der Klis, M. 1994, APJS, 92, 511

van der Klis, M., Swank, J. H., Zhang, W., Jahoda K., Morgan, E. H., Lewin, W. H. G., Vaughan, B., van Paradijs, J. 1996, ApJL, 469, L1

Zhang, S. N., Wilson, C. A., Harmon, B. A., Fishman, G. J., Wilson, R. B., Paciesas, W. S., Scott, M., Rubin, B. C. 1994, IAU Circ. 6046

Zhang, S. N., Robinson, B. A., Harmon, B. A., Paciesas, W. S., Fishman, G. J. 1996, IAU Circ. 6411

Zhang, W., Jahoda, K., Swank, J. H., Morgan, E. H., & Giles, A. B. 1995, ApJ, 449, 930

Table 1: Summary of pointed *RXTE* observations of GRS 1915+105.

Date[a] Start–End (1996;UT)	Exposure[b] Time (ks)	Mean[c] Intensity (Crab)	Hardness[d] Ratio	RMS Intensity[e] Variation (%)	QPO[f] Centroid (Hz)
April 06 05:39–07:51	5.6	1.5	1.1	35.3	0.0016, 0.12
April 09 16:47–21:43	10.1	1.6	1.0	11.4	0.159
April 17 13:51–18:50	6.0	1.4	1.2	13.5	0.0157, 0.1
April 20 10:31–16:06	8.7	1.5	1.4	10.6	0.019, 0.059
April 29–30 20:15–00:27	8.0	1.0	1.0	12.2	0.015, 0.12
May 05 13:59–18:00	9.9	1.3	1.3	11.2	0.067[g],0.8
May 14 15:43–19:53	10.0	1.0	1.3	15.1	0.012, 0.11[h], 7.6
May 21 01:45–02:23	2.3	2.3	1.1	37.3	
May 26 17:29–20:03	6.8	1.6	1.2	52.9	
May 29 12:43–15:12	5.9	0.7	1.2	8.4	1.9
May 31 11:25–16:55	10.6	0.8	1.1	10.3	1.9
June 05 11:34–17:39	10.9	0.9	1.1	10.5	1.6
June 07 09:38–15:22	11.0	1.0	1.1	12.0	1.5
June 12 00:07–14:53	11.0	2.0	1.1	23.9	
June 16 14:33–22:43	12.0	1.1	1.3	41.7	0.003, 5.1
June 19 14:36–21:37	10.7	1.2	1.1	45.7	
June 22 14:39–22:04	9.2	1.0	1.1	24.5	
June 25 01:54–15:16	10.6	1.2	1.1	25.7	
June 29 13:11–20:33	9.1	0.4	1.2	7.9	
July 03 08:27–12:29	6.4	0.6	0.9	9.8	
July 06–07 23:22–22:16	6.4	1.2	1.0	34.9	8.0
July 11 02:09–10:11	9.7	0.8	1.1	15.1	2.6–3.5[i]
July 14 11:47–15:58	10.1	0.9	1.3	14.4	3.6–4.2[i]
July 16 04:03–08:53	10.0	0.8	1.4	16.4	2.3–2.5[i]
July 19 11:51–16:02	10.3	0.7	1.8	17.3	1.1[h]
July 26 13:50–17:43	9.4	0.7	2.0	16.7	0.65[h]
August 03 12:49–17:51	11.2	0.7	1.9	17.3	0.9[h]
August 10 08:56–13:09	10.2	0.7	1.6	17.2	1.7–2.0[h,i]
August 18 07:20–11:42	10.6	1.1	1.2	18.4	4.6–5.6[i]
August 25 04:41–08:35	9.5	0.9	1.2	16.3	3.5–4.5[i]
August 31 07:48–11:14	7.6	1.5	1.2	19.5	5.7-6.6[i]

[a] The start and end times of the observation. [b]The total exposure time in kilo-seconds.

[c]The mean intensity in unit of the Crab (the count rate per PCU/2500).

[d]The hardness ratio (5.2 – 60/2 – 5.2 keV).

[e]The total RMS variability, defined as the square root of the integrated power between 0.1mHz and 100 Hz.

[f] The centroid frequency of the most prominent QPO features.

[g]The first 3 harmonics of this line are clearly visible.

[h]First Harmonic also seen.

[i]The centroid frequency varied in this range over the observation.

Table 2: Parameters of the 67 Hz QPO

Date	Line Center (Hz)	Line Width (Hz)	RMS Amplitude (%)
April 06	67.1 ± 1.1	3.4 ± 4.0	0.72 ± 0.44
April 20	67.7 ± 0.3	3.6 ± 0.7	1.06 ± 0.16
April 29	66.2 ± 0.5	3.3 ± 1.1	0.90 ± 0.24
May 05	65.5 ± 0.2	4.4 ± 0.6	1.63 ± 0.17
May 14	66.8 ± 0.8	2.9 ± 2.4	0.80 ± 0.39
June 11	64.9 ± 0.4	2.0 ± 1.1	0.47 ± 0.17

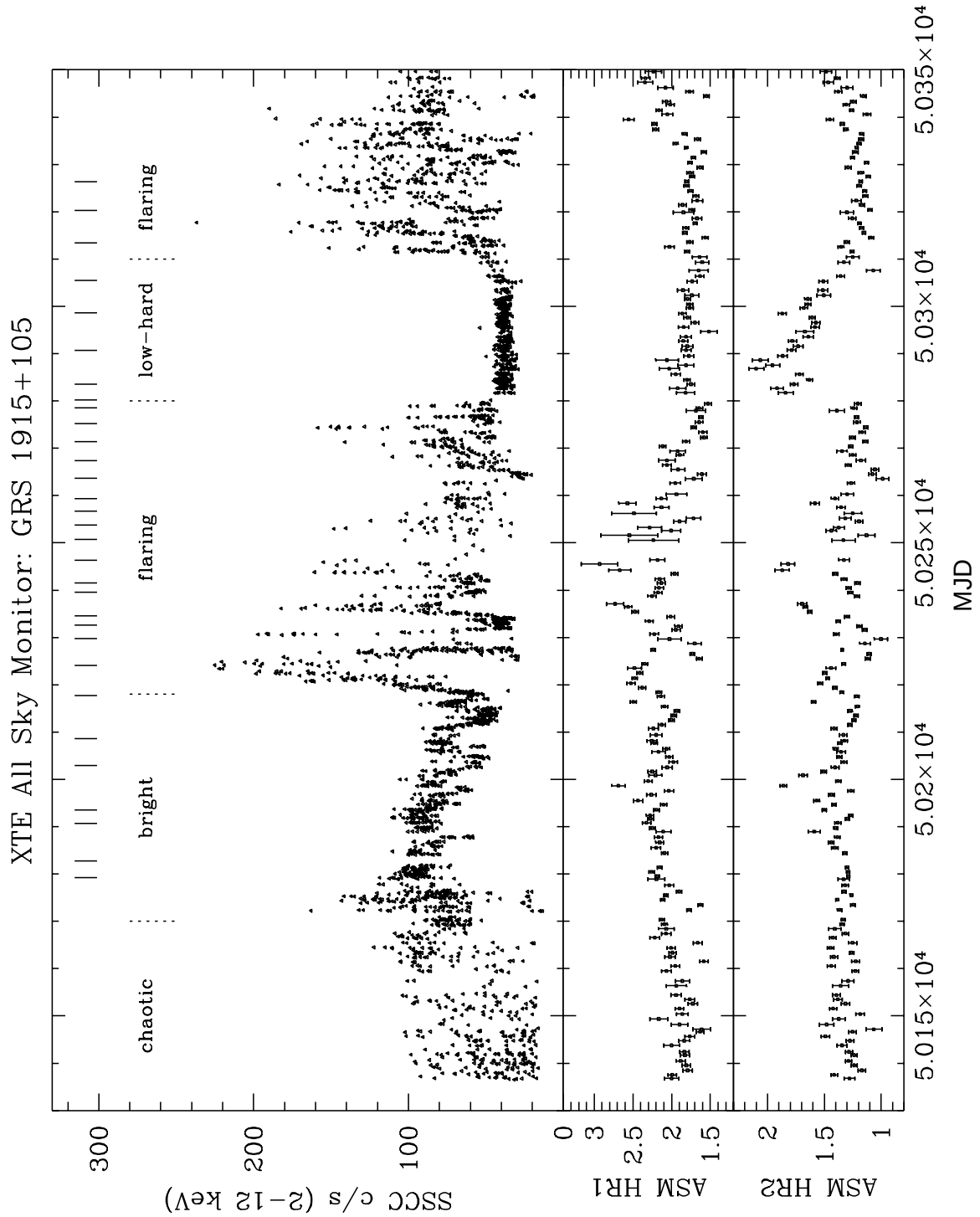

Fig. 1.— Light curve of GRS 1915+105 between 1996 Feb. 17 and 1996 Sept. 24, as measured with the RXTE/ASM in the 2–12 keV range (top panel). The lower panels show the ASM spectral hardness ratios, defined as HR1 = 3–5 keV flux / 1.2–3 keV flux and HR2 = 5–12 keV flux / 3–5 keV flux.

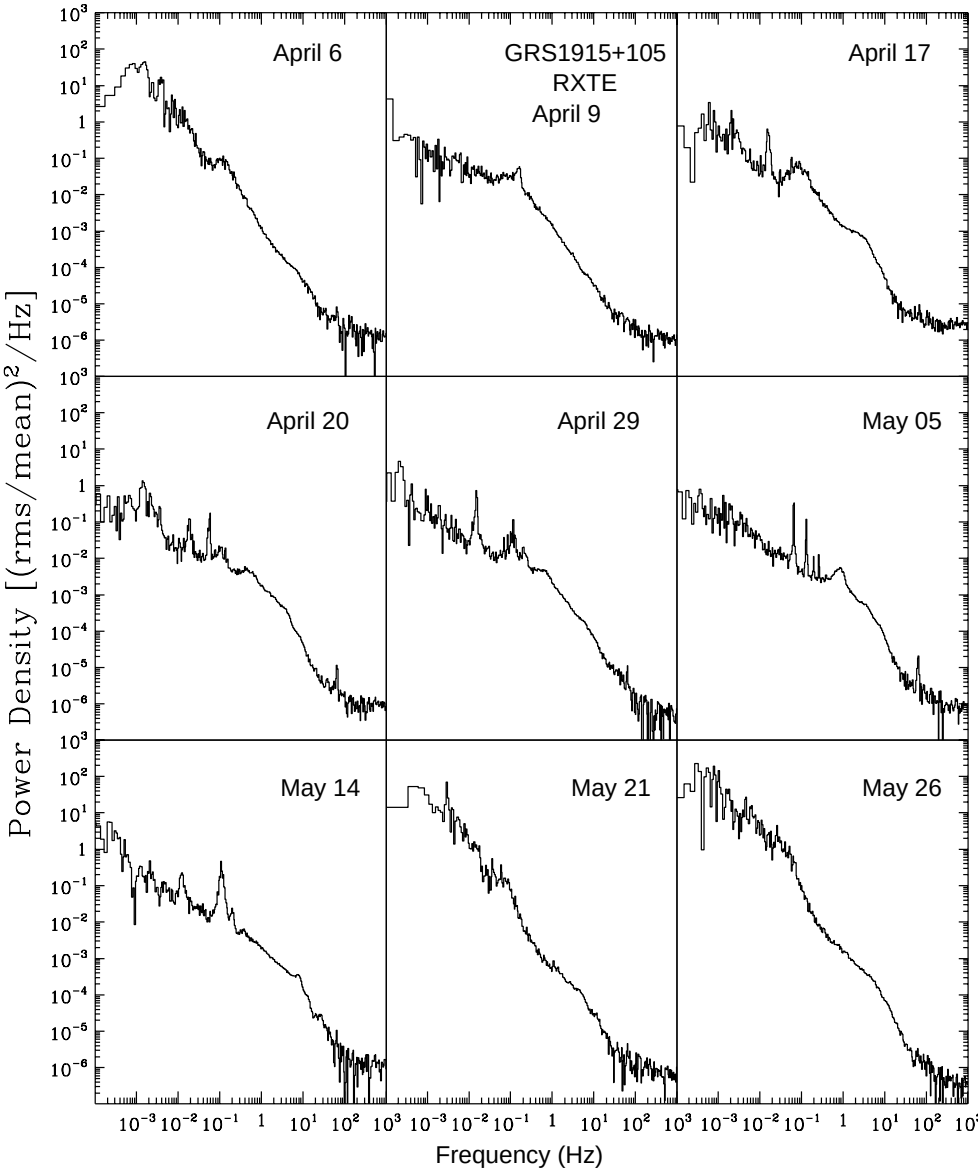

Fig. 2.— Power spectra of GRS1915+105 computed from *RXTE* PCA observations effectively sampling the range of 2-20 keV. The Poisson noise level, corrected for instrumental deadtime, has been subtracted.

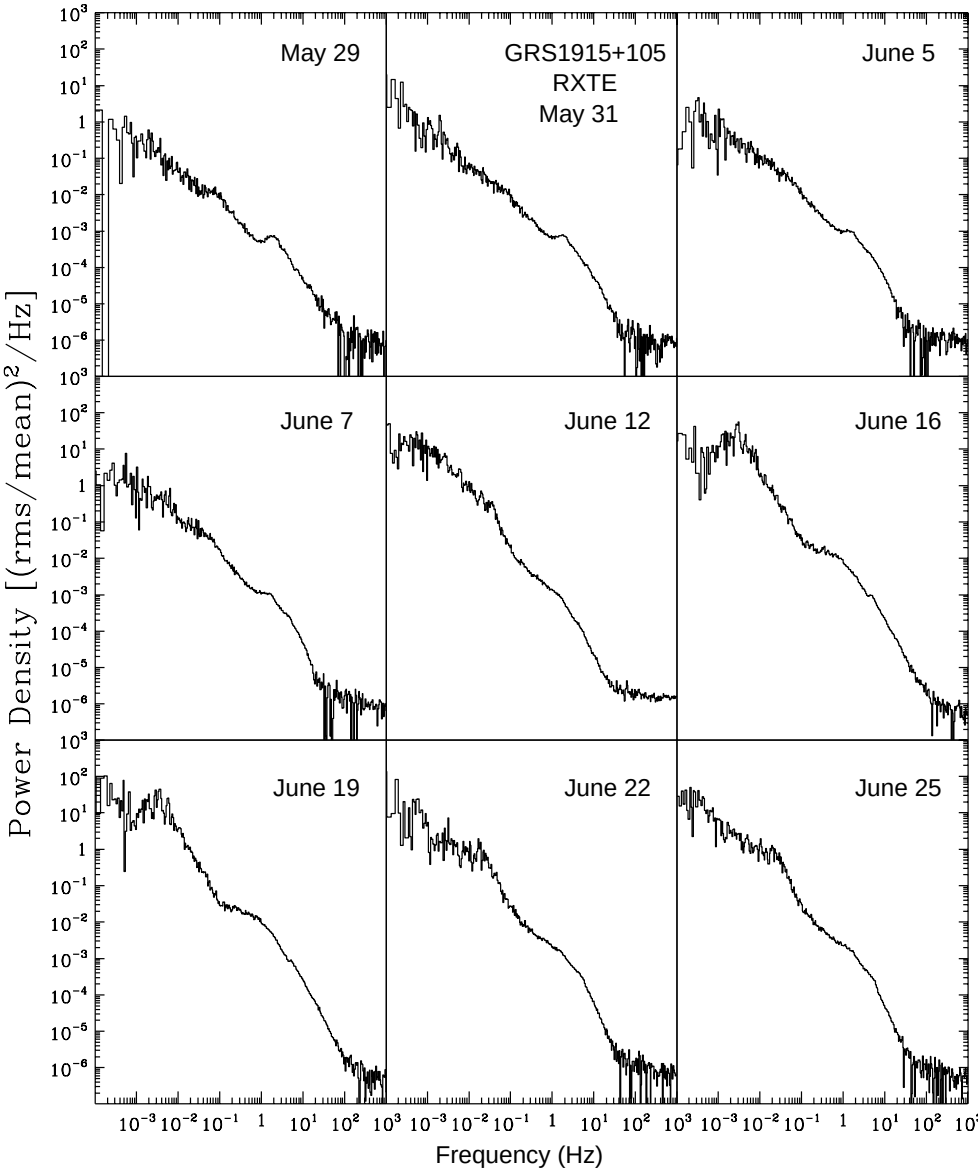

Fig. 3.— Power spectra of GRS1915+105 computed from *RXTE* PCA observations effectively sampling the range of 2-20 keV. The Poisson noise level, corrected for instrumental deadtime, has been subtracted.

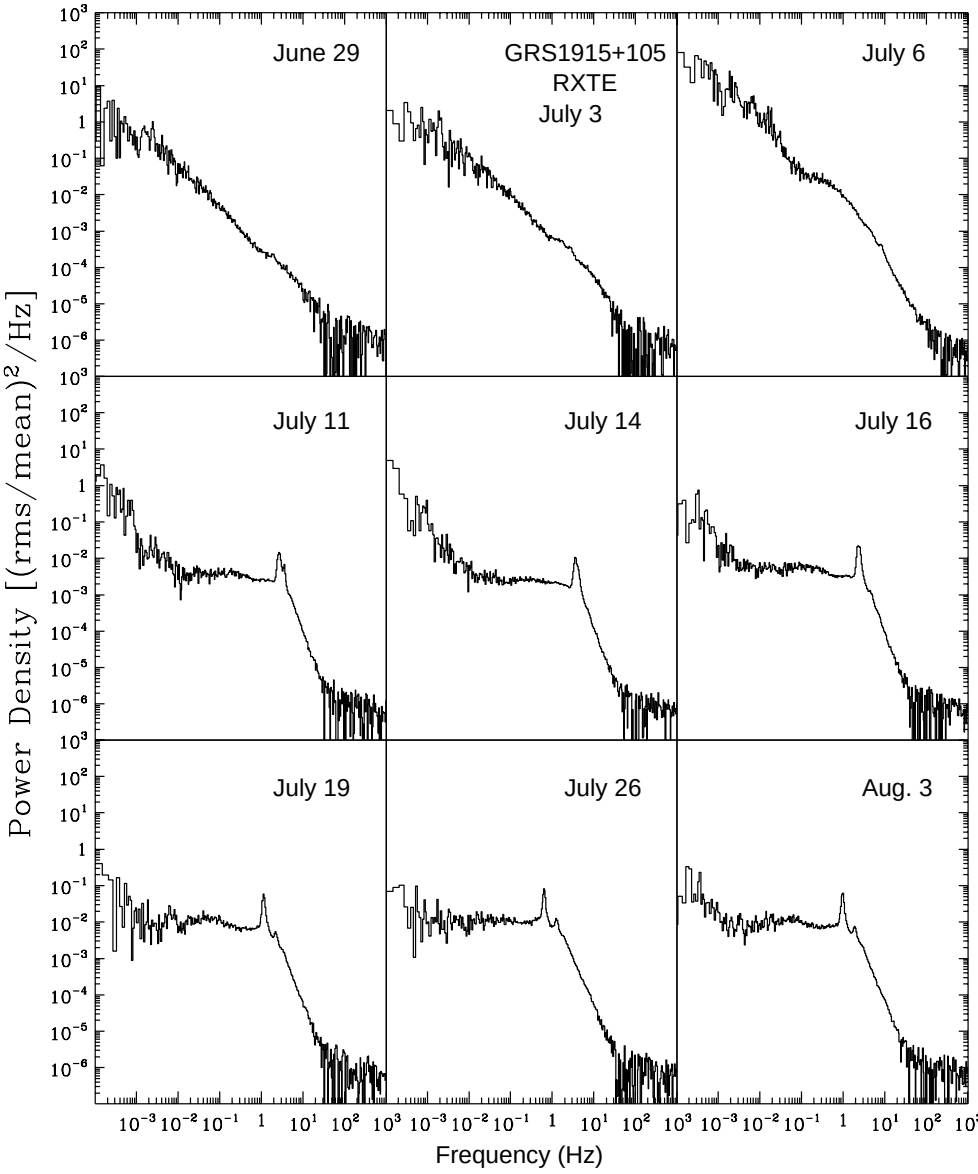

Fig. 4.— Power spectra of GRS1915+105 computed from *RXTE* PCA observations effectively sampling the range of 2-20 keV. The Poisson noise level, corrected for instrumental deadtime, has been subtracted.

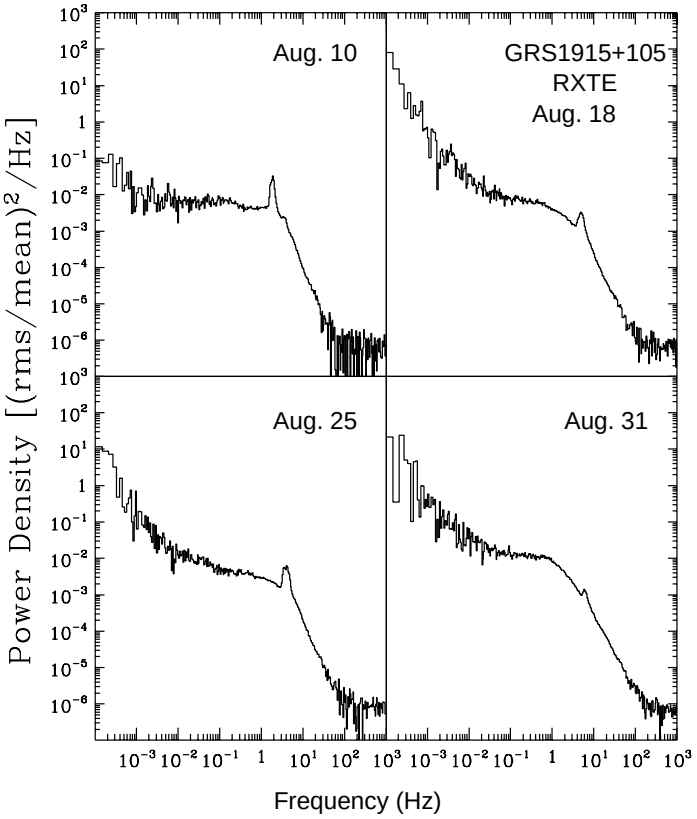

Fig. 5.— Power spectra of GRS1915+105 computed from *RXTE* PCA observations effectively sampling the range of 2-20 keV. The Poisson noise level, corrected for instrumental deadtime, has been subtracted.

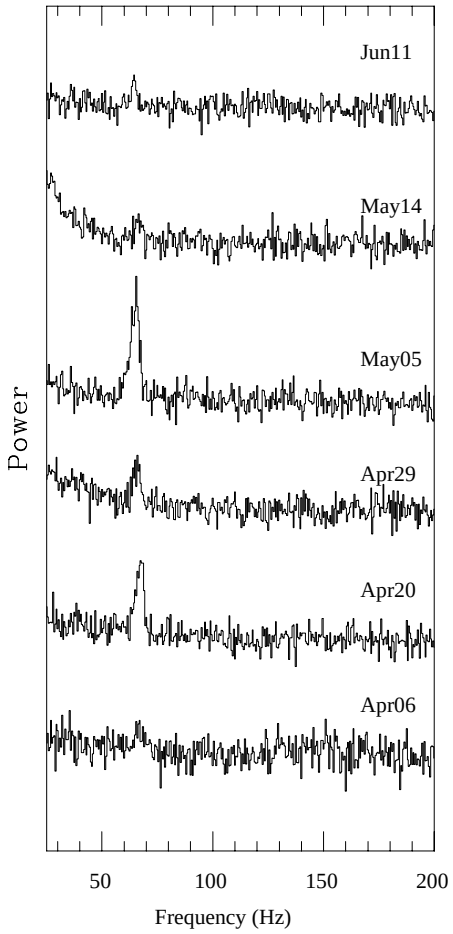

Fig. 6.— Selected power spectra of GRS1915+105 replotted on a linear scale to display the QPO at 67 Hz. Here the Poisson noise level has not been subtracted.

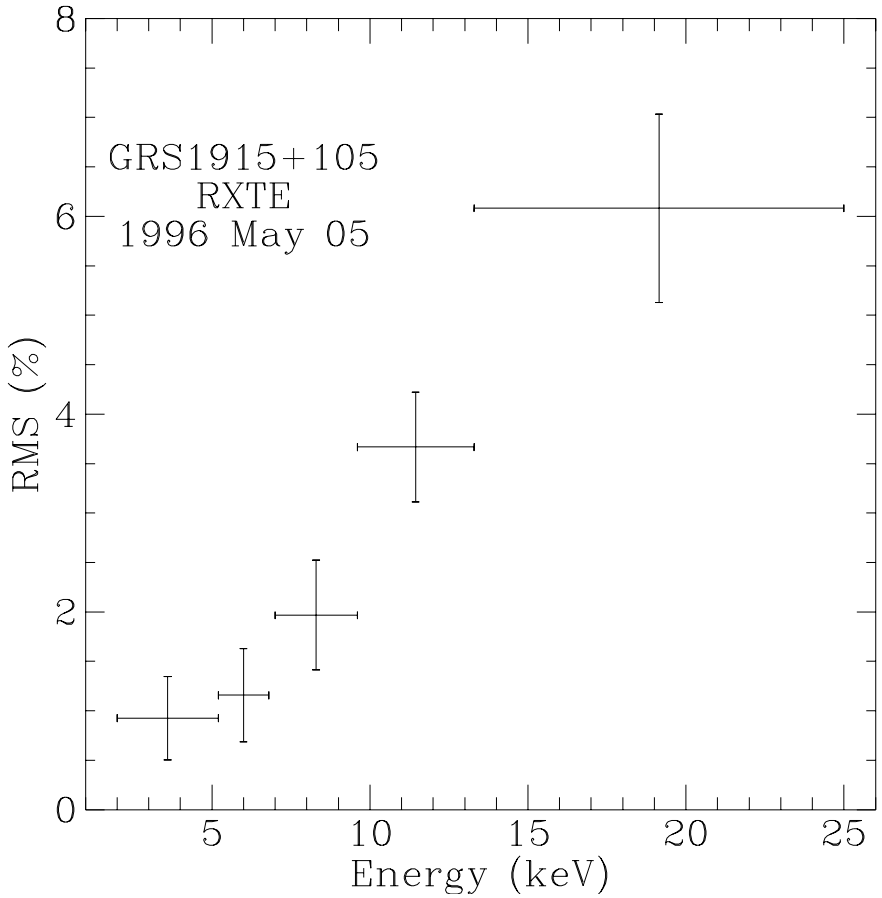

Fig. 7.— Energy dependence of the 67 Hz QPO, shown in the relation between the integrated QPO feature in the power spectrum vs. the mean photon energy, in 5 intervals of PCA energy channels.

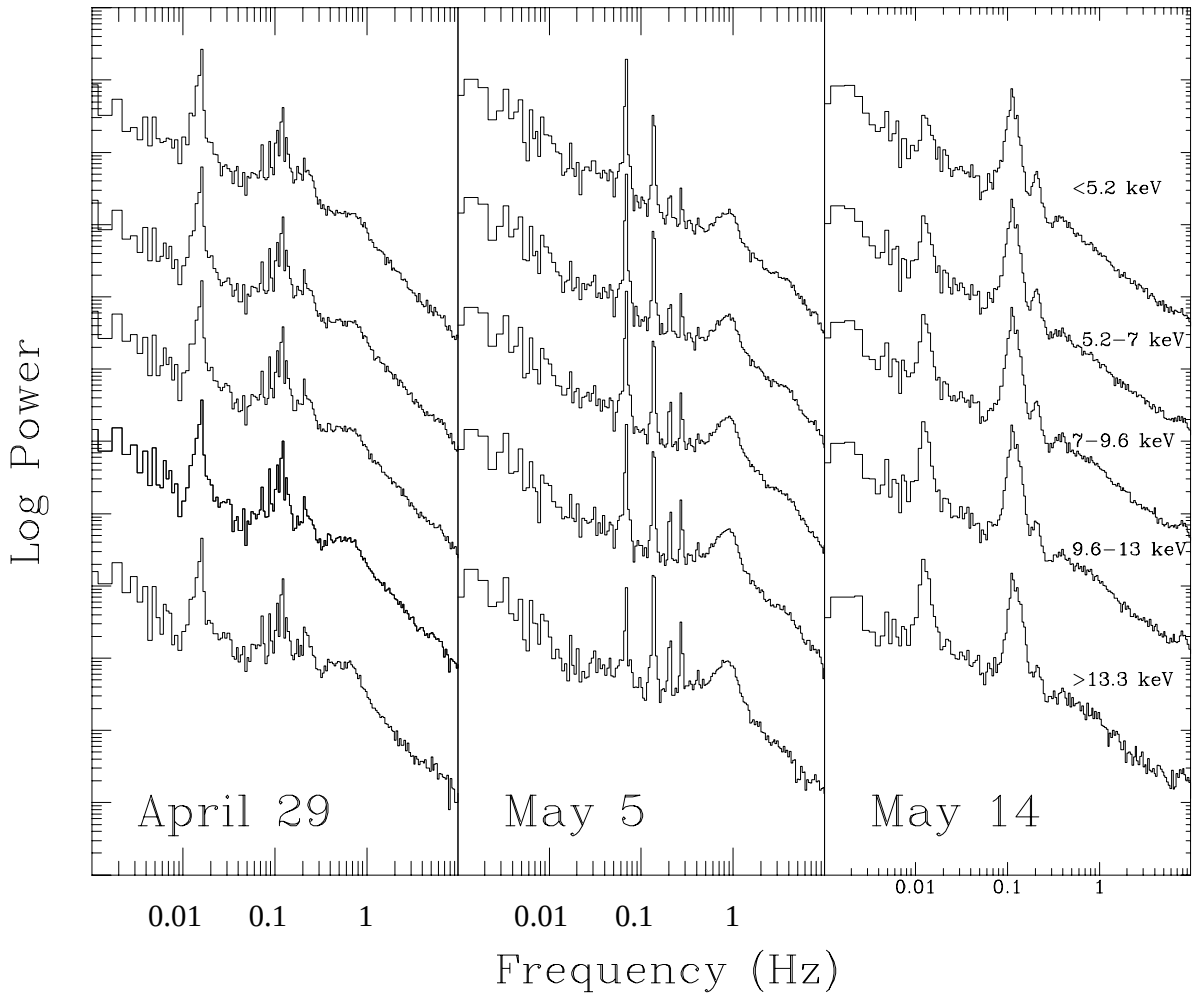

Fig. 8.— Energy-resolved power spectra highlighting samples of the high-Q QPO displayed in Figure 1a. The five energy ranges are given in the May 14 panel. Note the quantized appearance of QPO near 0.1 Hz on April 29. On May 5 the harmonics of the 0.07 Hz QPO increase with higher energy, while on May 14 the first harmonic of the broader QPO at 0.11 Hz decreases with higher energy. On May 14 the QPO at 0.012 Hz appears strongly enhanced at higher energies.

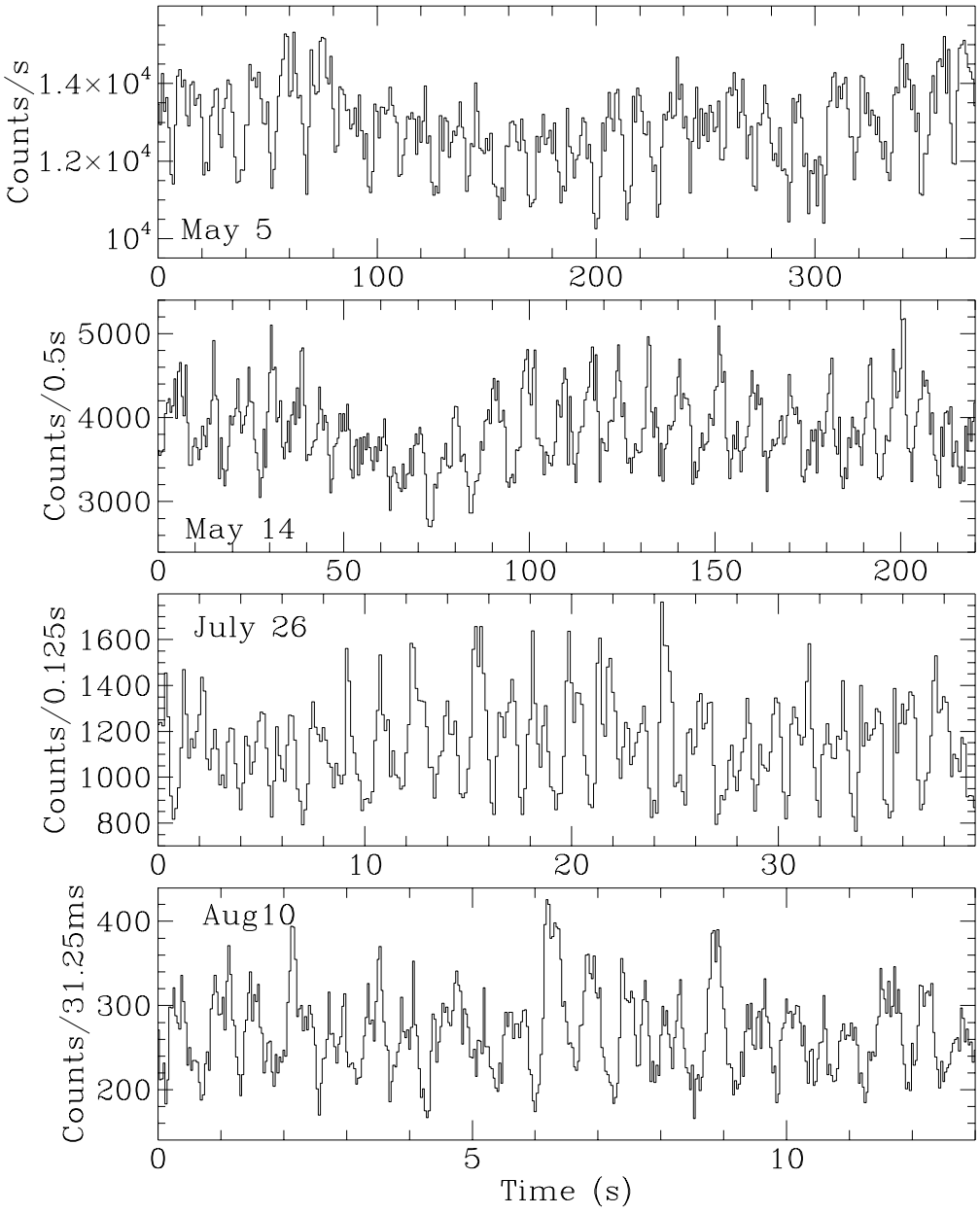

Fig. 9.— Sample light curves showing individual QPO oscillations during four observations of GRS1915+105 with the PCA. Each panel shows 25 QPO cycles.

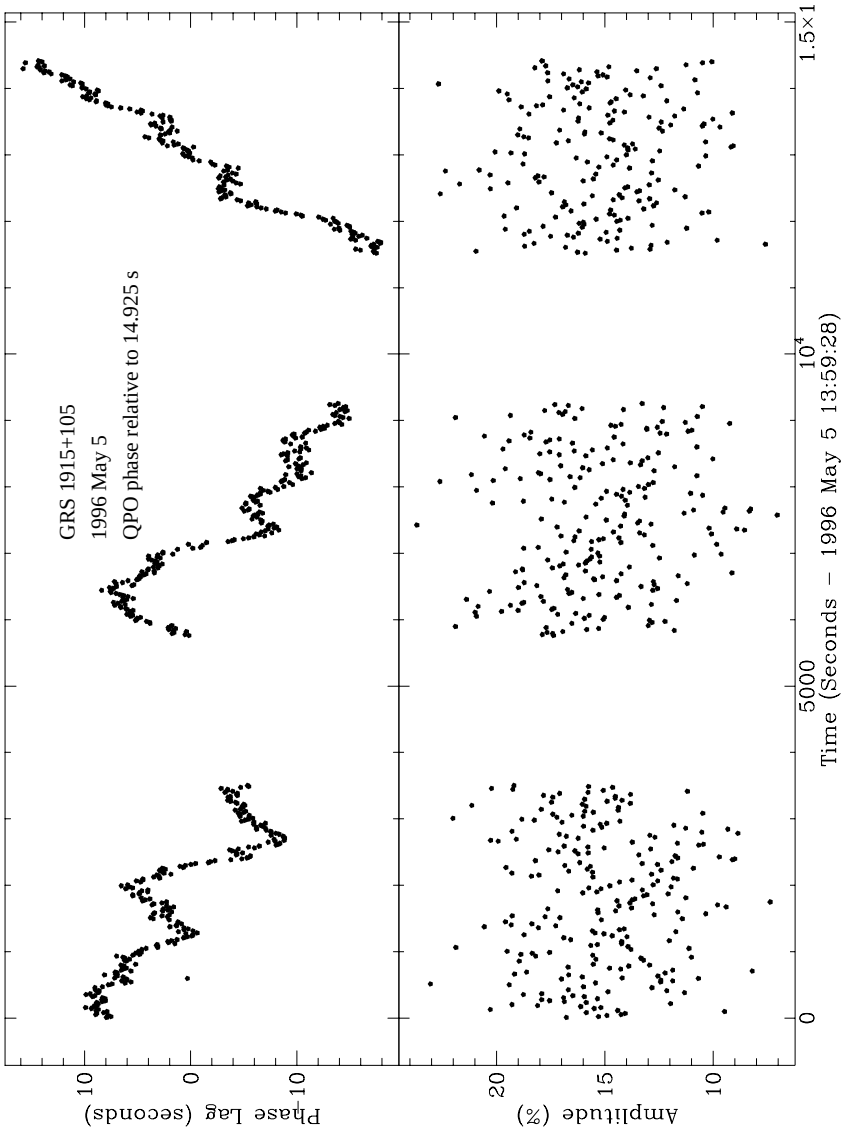

Fig. 10.— QPO monitor for the 0.067 Hz narrow QPO seen on May 5. The top panel tracks the arrival times of individual QPO waves, modulo 14.925 s. At the beginning of each exposure segment, the phase of the first wave is arbitrarily set to match the last wave in the previous segment. Note that any single phase jump near 0.5 (7.5 s) is ambiguous. In the bottom panel the amplitudes of these QPO are shown as a percentage of the mean rate. In this case the QPO template is a 3 s dip that resembles the mean QPO profile.

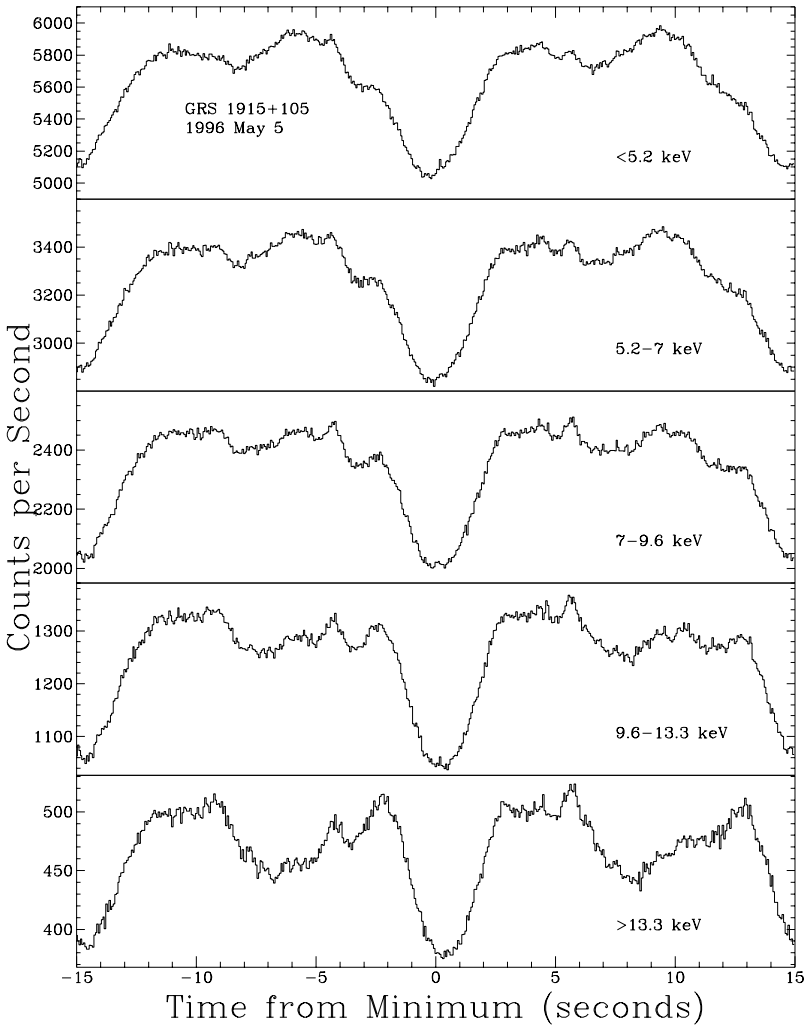

Fig. 11.— Average QPO-folded profile for the 0.067 Hz narrow QPO seen on May 5. The dips are shown in the 5 energy bands given in Figure 4. Note the sharpness of the dips and the secondary minimum at high energies. There is clearly a time delay that increases with energy.

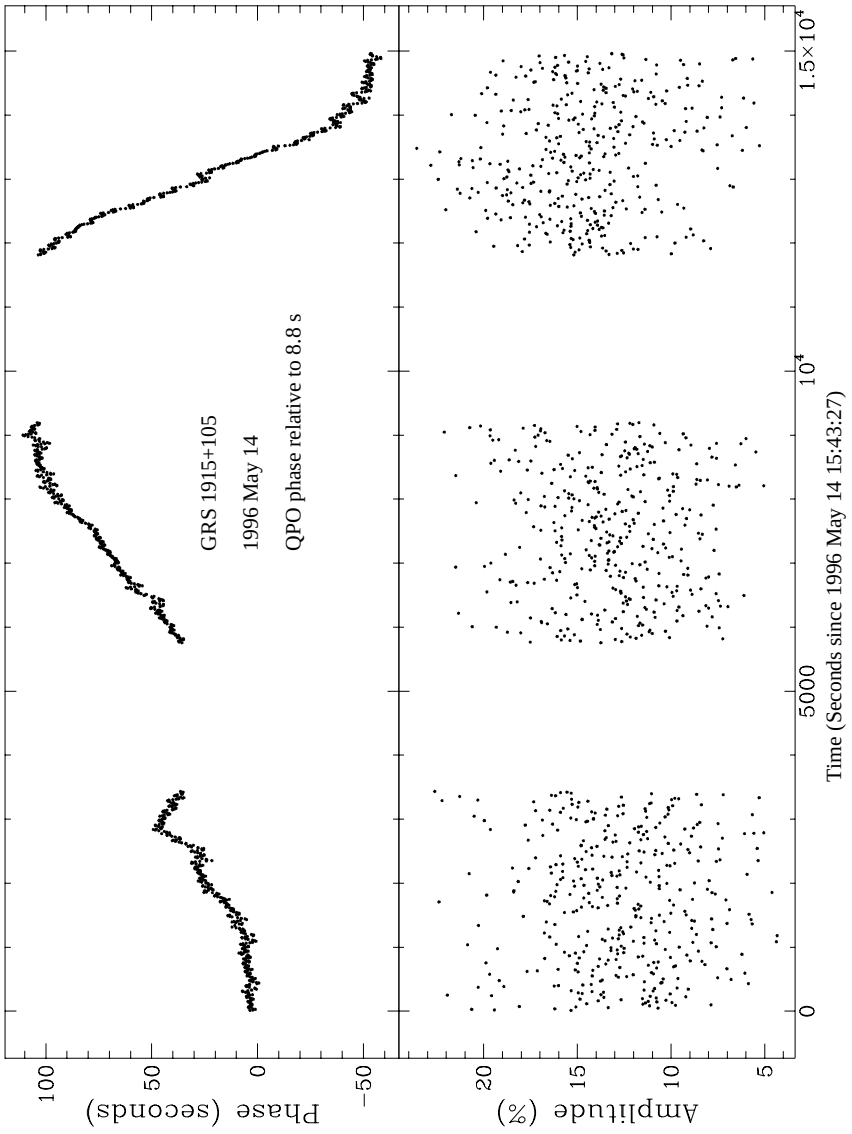

Fig. 12.— QPO monitor for the 0.11 Hz QPO seen on May 14. The top panel tracks the arrival times of individual QPO waves, modulo the QPO centroid time scale of 8.80 s. At the beginning of each exposure segment, the phase of the first wave is arbitrarily set to match the last wave in the previous segment. Note that any single phase jump near 0.5 (4.4 s) is ambiguous. In the bottom panel the amplitudes of these QPO are shown as a percentage of the mean rate. In this case the QPO template is a sine wave and the amplitude is measured peak-to-peak.

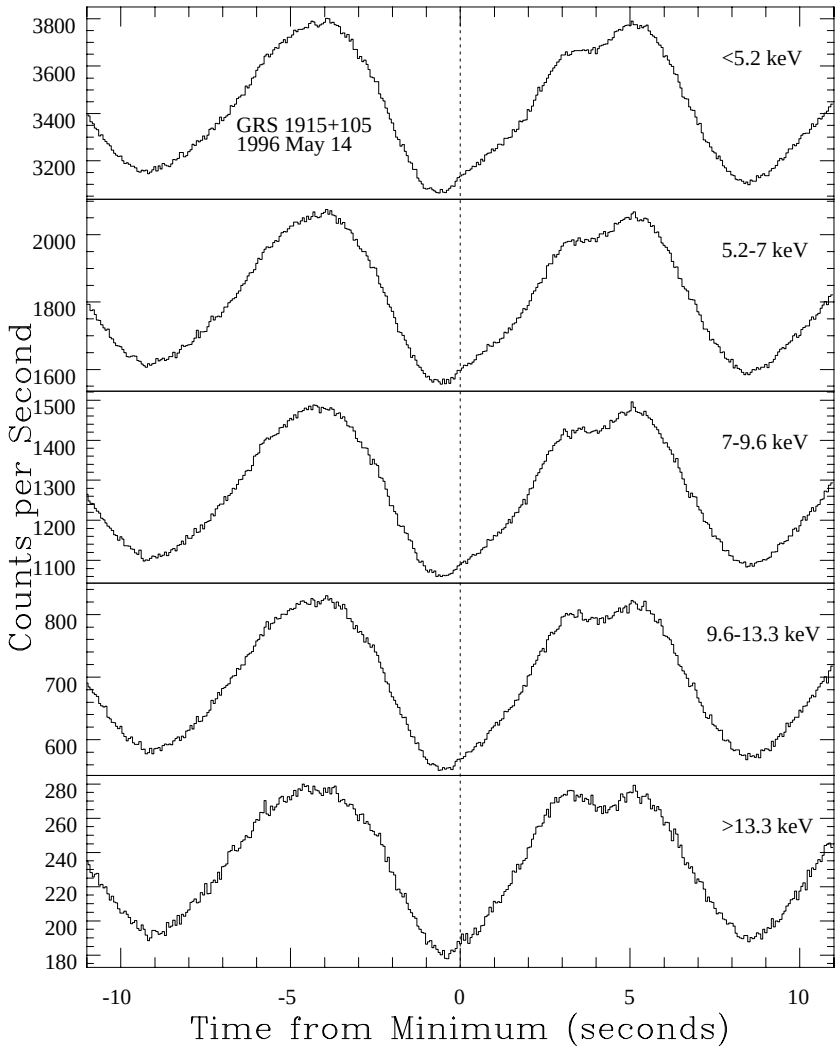

Fig. 13.— Average QPO-folded profile for the 0.11 Hz QPO seen on May 14. The mean wave form appears sinusoidal in each of the 5 energy bands (as given in Figure 4). Again there is a phase lag, with a delay of 0.017 between 3 and 15 keV.

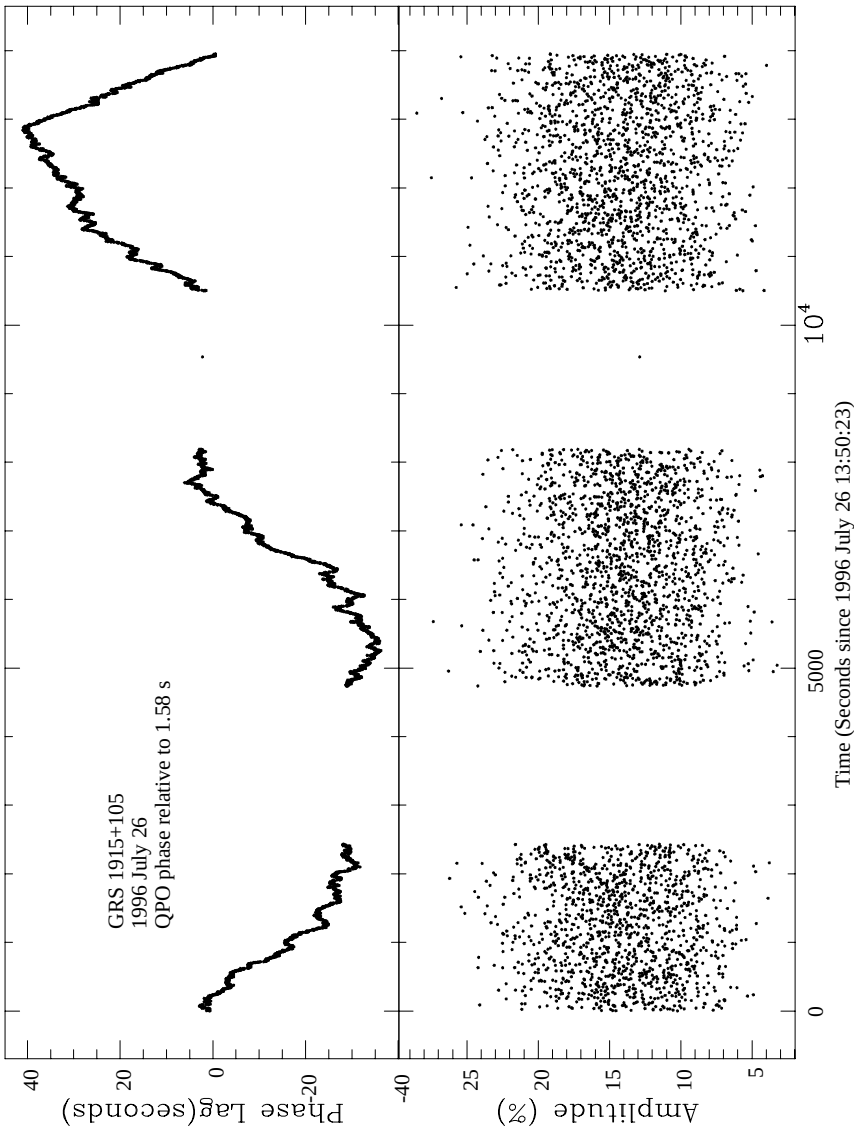

Fig. 14.— QPO monitor for the 0.63 Hz narrow QPO seen on July 26. The QPO arrival phases were calculated relative to a period of 1.58 s. The QPO amplitudes are modeled with a sine wave, and they are given as peak-to-peak measurements.

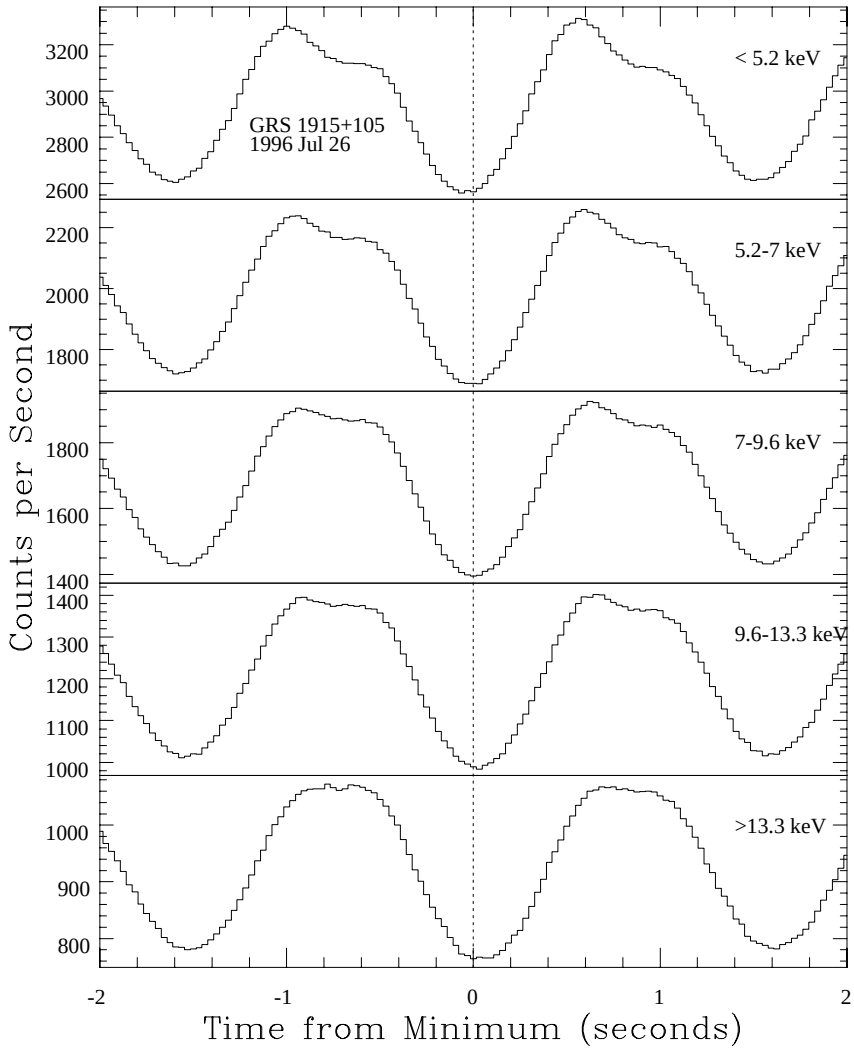

Fig. 15.— Average QPO-folded profile for the 0.63 Hz QPO seen on July 26. The mean wave form is again sinusoidal in each of the 5 energy bands (see Figure 4). The results are very similar to those in Figure 8, including a phase lag of 0.033 between 3 and 15 keV.